Histology Image Classification, Retrieval Using Extracted Local Features from Circularly Surrounded Neighbors

Hamed Erfankhah
Department of Electrical and Biomedical Engineering, Ur.c., Islamic Azad University, Urmia, Iran.
Email: erfankhah_hamed@iau.ac.ir
Receive Date: 07 June 2025 Revise Date: 30 June 2025 Accept Date: 20 July 2025

Abstract

With the rapid advancement of digital imaging technologies, histology image analysis has become increasingly important in medical research and clinical diagnosis. Histology images are widely used for both educational purposes and disease detection, particularly in oncology. Computer-aided diagnosis systems offer valuable support to pathologists by automating image analysis and retrieving visually similar cases for comparison. In this study, a content-based image retrieval and classification framework is proposed using handcrafted texture features extracted from histopathological images. The method incorporates rotation-invariant uniform Local Binary Pattern (LBP), first and second statistical moments, and Local Variation Code (LVC) features computed over circular neighborhoods with multiple radii. These features are designed to capture local micro-patterns while being invariant to rotation and grayscale variations. The performance of the proposed approach was evaluated using two publicly available histopathology datasets: Kimia Path24 and BreakHis. Experimental results showed that even individual feature types can achieve high classification accuracy on one of the datasets. Moreover, combining different feature sets further improved performance, especially in modeling fine-grained structural differences. To enhance discriminative power and reduce redundancy, several optimal feature selection techniques were applied. The resulting low-dimensional feature representation not only improves computational efficiency but also outperforms previously reported methods in terms of retrieval and classification accuracy on the tested datasets.

Keywords: Whole Slide Image (WSI), Content-Based Image Retrieval (CBIR), Local Features, Feature Selection.

1. Introduction

Histopathological images, which capture the microscopic structure of tissues, play a critical role in modern medical science. These images are essential for understanding tissue morphology and identifying abnormal cellular changes, making them indispensable tools in disease diagnosis particularly in oncology, immunology, and infectious diseases. Histopathology enables pathologists to detect malignancies, assess tumor grades and stages, evaluate treatment responses, and provide prognostic information, all of which significantly support clinical decision-making [1]. A major advancement in this field is the development of Whole Slide Imaging (WSI) technology, which allows the digitization of entire histopathological slides at high resolution [2]. WSI systems convert glass slides into digital images that can be viewed, analyzed, and shared electronically. This innovation has transformed traditional microscopy into a more efficient, scalable, and collaborative process, enabling remote diagnosis, telepathology, and integration with computational analysis tools [3]. In recent years, Artificial Intelligence (AI) especially machine learning and deep learning techniques has emerged as a powerful tool for analyzing these large-scale digital histopathological images. AI-based models can automate the detection, classification, and segmentation of tissue

regions, offering consistent and accurate interpretations [4]. These systems help identify subtle patterns that may be missed by human observers, reduce inter-observer variability, and ultimately improve diagnostic reliability [5]. Moreover, computer-aided frameworks enable efficient content-based image retrieval, early disease detection, prognosis prediction, and discovery of novel biomarkers by analyzing vast repositories of digitized histopathological data [6]. As these technologies continue to evolve, their integration into histopathology promises to enhance both research and clinical practice by increasing efficiency, accuracy, and accessibility in healthcare.

Computer-aided systems widely utilize two core techniques: image classification and content-based image retrieval. In classification tasks, whole slide images (WSIs) are analyzed to determine their association with specific pathological conditions or lesion subtypes [7]. Alternatively, retrieval methods focus on identifying and organizing images from extensive databases that exhibit comparable visual traits—such as chromatic properties, textural patterns, and morphological structures to a given query image [8]. By retrieving previously diagnosed cases with similar characteristics, these systems can provide valuable context and support for pathologists in the diagnostic process.

Among various handcrafted feature extraction techniques, the Local Binary Pattern (LBP) has demonstrated significant advantages in histopathological image analysis compared to other widely used descriptors such as Scale-Invariant Feature Transform (SIFT) , Speeded-Up Robust Features (SURF) , and Histogram of Oriented Gradients (HOG) [9-11].

Unlike SIFT and SURF, which are primarily designed for keypoint detection and matching in natural images, LBP focuses on capturing local texture patterns, which are highly relevant in histopathological images where tissue structures and cellular arrangements often exhibit subtle variations in texture rather than shape or gradient orientation [4]. Moreover, SIFT and SURF are computationally more expensive and may not perform consistently well under the high-resolution and complex staining conditions typical of histopathology slides [12].

On the other hand, HOG, which captures edge and gradient orientation distributions, is effective for object detection in natural scenes but may overlook fine-grained textural differences that are crucial in distinguishing between benign and malignant tissues [6]. In contrast, LBP offers a compact and efficient representation of local textures, while being robust to illumination variations a common issue in digitized histopathology images due to inconsistent staining and scanning conditions [4]. Additionally, LBP-based features can be extended to multi-scale and rotation-invariant variants, making them highly adaptable for analyzing histological patterns regardless of tissue orientation. This property is particularly valuable in whole slide images (WSIs), where structural orientation may vary across different regions of interest [13].

In summary, while SIFT, SURF, and

HOG have their strengths in general image analysis tasks, LBP provides a more suitable and effective feature representation for histopathological image classification and retrieval, especially when the diagnostic clues lie in the micro-texture properties of tissue samples [14].

In this study, a set of rotation-invariant and grayscale-stable texture descriptors were employed to capture fine local structures in histopathological images. These descriptors include uniform Local Binary Patterns (LBP), as well as statistical features such as first- and second-order moments and local variation codes, all computed over multiple circular neighborhoods with varying radii. Different combinations of these features were evaluated to identify the most effective configuration for image characterization.

Furthermore, feature selection techniques were applied to the best-performing combined representation in order to eliminate redundant information and retain only the most informative features. This not only reduces the overall dimensionality of the feature space but also enhances retrieval performance by focusing on discriminative patterns.

The core idea behind the proposed approach lies in its ability to model subtle micro-structural arrangements within tissue samples. This is achieved by encoding spatial distributions of local textures using histogram-based representations.

The method was tested on two publicly accessible histopathological image datasets including Kimia Path24 and BreakHis where it demonstrated promising results in both classification and content-based retrieval tasks.

2. Research Method

This work focuses on utilizing local texture descriptors to effectively characterize the visual content of histopathological images. A set of grayscale-invariant and rotationally robust features was employed to capture fine-scale structural patterns within tissue samples. These descriptors were extracted from localized regions and subsequently combined into a comprehensive feature representation.

The selected texture features are based on analyzing pixel intensity variations within circular neighborhoods defined by different radius (R) and number of surrounding pixels (P), referred to as the (P, R) configuration. To account for multi-scale characteristics, multiple configurations were considered, and their corresponding features were integrated to enhance descriptive power. Below is an overview of the key texture descriptors used in this study:

(1) **Rotation invariant local binary patterns feature:**

This descriptor provides a compact representation of local texture by comparing the intensity of a central pixel with its neighboring pixels arranged in a circular pattern [13]. The resulting binary values are converted into a decimal code that remains consistent under image rotation. The general form of the LBP operator for a neighborhood defined by (P, R) is calculated using the following expression:

$$LBP_{P,R} = \sum_{p=0}^{P-1} s(g_p - g_c)2^p \quad (1)$$

where

$$s(x) = \begin{cases} 1 & x \geq 0 \\ 0 & x < 0 \end{cases} \quad (2)$$

The intensity of the central pixel (g_c) within a local region is compared with the gray-level values of its neighboring pixels (g_p), which are positioned uniformly around it on a circular path defined by radius R (where R>0) and indexed by p=0,…,P−1. These P surrounding pixels together form a rotationally symmetric neighborhood configuration. An extended variant of the LBP operator, known as rotation-invariant uniform pattern encoding, was employed in this study. This approach reduces the dimensionality of the feature space by focusing on texture patterns that exhibit a limited number of binary transitions either from 0 to 1 or from 1 to 0 along the circular arrangement of neighboring pixels. The concept of "uniformity" refers to the consistency in the binary structure of the LBP code, where only a small number of intensity changes occur around the local neighborhood.

According to the findings reported by Ojala et al. [15], such uniform patterns account for the majority of observed textures, with more than 90% occurrence in the commonly used (8,1) configuration. These rotationally robust and uniform features can be effectively extracted within any (P, R) neighborhood to enhance both efficiency and descriptive capability.

$$LBP_{P,R}^{riu2} = \begin{cases} \sum_{p=0}^{P-1} s(g_p - g_c) & if\ U(LBP_{P,R}) \leq 2 \\ P+1 & otherwise \end{cases} \quad (3)$$

Where $U(LBP_{P,R})$ refers to uniform LBP pattern in (P,R) and can be computed as:

$$U(LBP_{P,R}) = \left| s(g_{P-1} - g_c) - s(g_0 - g_c) \right| + \sum_{p=1}^{P-1} \left| s(g_p - g_c) - s(g_{p-1} - g_c) \right| \quad (4)$$

Once the LBP codes are generated for the input image, a histogram is constructed based on the frequency of uniform patterns across the image. This histogram captures the statistical distribution of these texture features and serves as a compact representation of the image's local structural properties.

(2) **First and Second-Order Statistical Features:**

To capture local statistical characteristics, such as average intensity and contrast variations, the first-order moment (mean, M) and second-order moment (variance, V) were computed over the pixel values within each (P, R) neighborhood. These measures provide quantitative insights into the distribution of grayscale levels across local image regions, and are defined as follows:

$$M = \frac{1}{P} \sum_{p=1}^{P} g_p \quad (5)$$

$$V = \frac{1}{P} \sum_{p=1}^{P} (g_p - M)^2 \quad (6)$$

The features derived from mean intensity and variance demonstrate invariance to both image rotation and grayscale shifts. To incorporate these properties into the feature representation, spatial histograms were generated based on the distribution of M and V values across the image. However, since these statistical measures are inherently continuous, they were first quantized into L discrete levels using the following approach:

$$QF = \frac{F - F_{\min}}{F_{\max} - F_{\min}} \times (L - 1) \quad (7)$$

where F(=M,V) is the feature that we want to quantize it and is the obtained quantized feature that is distributed in the range [0 L-1].

(3) Local variation code:

For neighborhood pixels in (P,R), the local variation bit (LVB) is computed as follows:

$$LVB = \begin{cases} 1 & if\ |g1 - g2| \geq T \\ 0 & otherwise \end{cases} \quad (8)$$

Where T is threshold, g1and g2 are local neighbors that have been located in the same direction with respect to the central pixel or on a same diagonal running through the center of the circle.

Putting together all the binary bits of each pairwise local neighborhoods, created a binary code which we called it local variation code (LVC).

The threshold value in the LVC can reduce the noise effect and extract features from non-homogeneous regions. For example, Fig.1 shows how the LVC feature is calculated in a (8, 1) neighborhood pixels:

For P members on a circle of radius R , the LVC has P/2 bits, and its decimal value can vary from 0 to 2^(P/2) – 1 . To reduce the length of the feature vector for greater values of P , only uniform and invariant LVC codes were extracted, and a histogram was used to count the number of occurrences of these uniform patterns in an image.

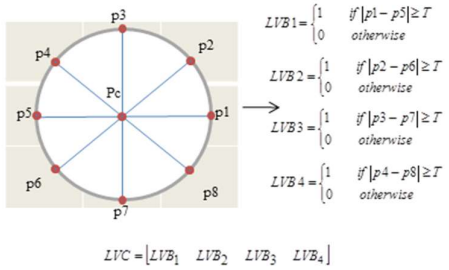

Fig.1. Extracting local variation code feature in a (8,1) neighborhood pixels.

LVC is invariant to grayscale image shifts. In order to make it rotation-invariant, one way is to calculate the LVBs according to the direction that has the greatest pixel intensity value (reference direction) and in the counter-clockwise direction.

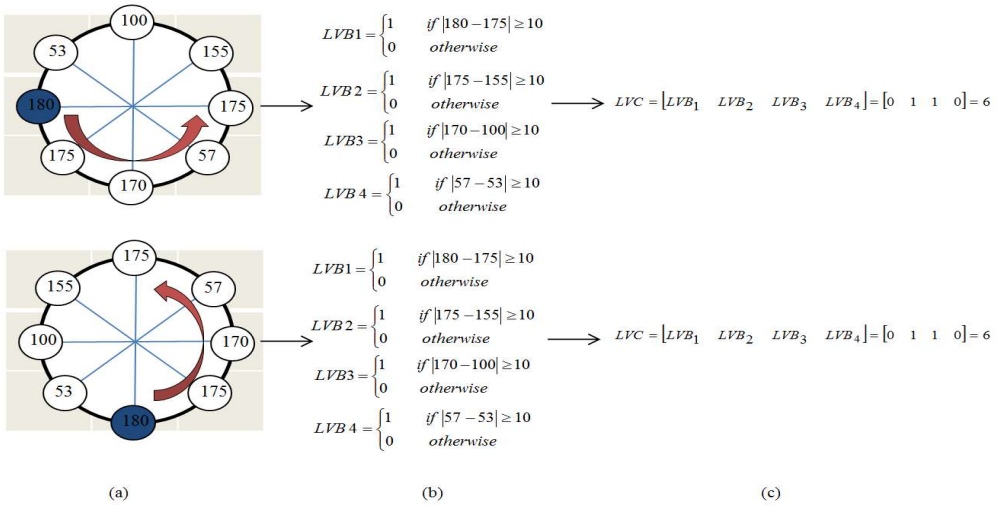

Fig.2. Rotation invariant LVC, (a) an example of neighborhood pixels in (8,1) (above) and its counter-clockwise rotation,(b) LVBs are calculated with respect to reference direction (blue circles in (a)) ,(c) Putting together all the LVBs in counter-clockwise and converting to decimal value.

In Fig. 2(a), the top image shows an example of neighborhood pixels in (8,1), and the bottom image shows neighborhood pixels that have been rotated counter-clockwise by a certain angle. For this example, we set T = 10 . The LVBs are calculated according to the reference direction (blue circle) and in the counter-clockwise direction, as shown in Figure 2(b). In Fig. 2(c), LVC is obtained by putting together all the LVBs and converting them into a decimal value. As we can see, the LVCs for the unrotated and rotated neighborhood pixels are the same. Another way is to rotate each pattern P times, and the minimum code over P rotations is preserved.

Fig.3 shows the feature extraction process for a thumbnail of histology image from Kimia path24 dataset. The image is divided into square blocks, and local features are extracted from each block.

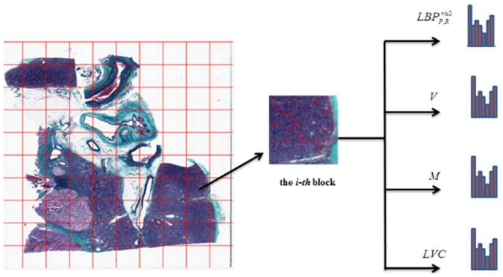

Fig.3. Feature extraction process for a thumbnail of histology image from Kimia path24 dataset.

3. Experiments

3. 1. Dataset

Kimia Path24 dataset- This dataset consists of 24 whole slide images, which have been manually selected from more than 350 scans, depicting the diverse body parts with distinct texture patterns [16]. The images were captured by Tissue Scope LE 1.0[1] in bright field using a 0.75 NA lens. For each image, one can determine the resolution by checking the description tag in the header of the file. For instance, if the resolution is 0.5µm, then the magnification is 20x, and if the resolution is 0.25µm, then the magnification is 40x. The number of test dataset has been fixed to facilitate benchmarking, the dataset contains 1325 test patches of size 1000 x 1000 (0.5mm X 0.5mm) from all 24 WSIs, but the number of the training dataset can vary according to preferences of the algorithm designer. Fig. 4(a) shows magnified portion of some samples in WSIs. The scans are available online and can be downloaded[2].

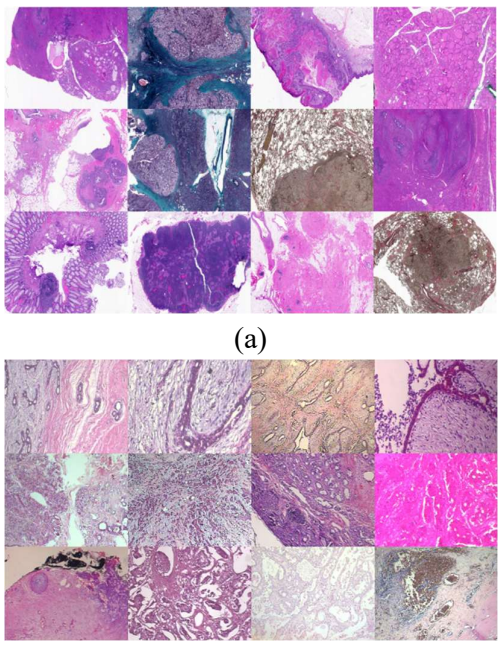

(a)

(b)

Fig.4. Some samples from (a) Kimia Path24, (b) BreakHis datasets.

[1] http://www.hurondigitalpathology.com/

[2] http://kimia.uwaterloo.ca

Table 1 presents the dimension and the number of testing patches of each WSI. To create training dataset, we considered two cases:

Table 1: Kimia path24 dataset: dimension and number of test patches of each WSI.

Scan Index	Dimension	Number of test patches
0	40300 × 58300	65
1	37800 × 50400	65
2	44600 × 77800	65
3	50100 × 77200	75
4	26500 × 13600	15
5	27800 × 32500	40
6	38300 × 51800	70
7	29600 × 34300	50
8	40100 × 41500	60
9	40000 × 50700	60
10	47500 × 84700	70
11	44100 × 52700	70
12	45400 × 60100	70
13	79900 × 56600	60
14	42800 × 58200	60
15	20200 × 57100	30
16	35300 × 46300	45
17	48700 × 61500	45
18	26000 × 49600	25
19	30700 × 70400	25
20	48200 × 81400	65
21	38500 × 40500	65
22	40500 × 45700	65
23	36900 × 4900	65

Case I. The WSIs are tiled into the patches of the same size as the test patches without any overlap. WSIs are large- scale images and some of these created patches do not have significant information and contain background pixels, therefore we used homogeneity criteria to preserve only patches that contain information and we calculated the homogeneity of each patch according to [17] as follows:

$$H = 1 - \frac{1}{L}\sqrt{\sum_i \sum_j (W_{ij} - m)^2} \qquad (9)$$

where W is the patch window, m is the median or the mean value of the pixels in the patch and L is the size of the patch.
Patches with homogeneity greater than 99% were removed, and a total of 25,979 non-overlapping patches of size 1000×1000 were extracted. Fig.5 shows the distribution of training samples in each WSI using green bars.

Case II. As presented in Table 1, the testing samples are relatively balanced, whereas the training samples are imbalanced, as evident from Fig.5. Certain WSIs contain significantly fewer training samples compared to others. To address this imbalance, the number of training samples for WSIs with limited data was increased through oversampling using overlapping tile patches. This process resulted in a total of 30,946 training sample patches. The distribution of training samples for this case is illustrated in Fig.4, represented by red bars.

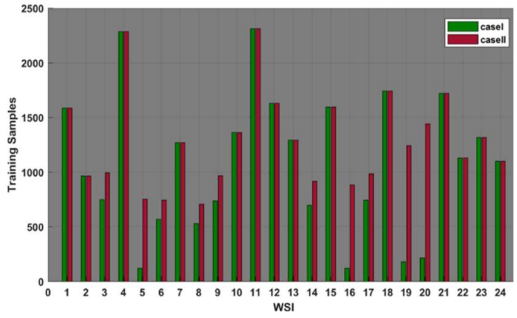

Fig.5. Distribution of training samples in Kimia Path24 dataset for case I and case II.

BreakHis dataset- The BreaKHis database contains microscopic biopsy images of benign and malignant breast tumors. Images were collected through a clinical study from January 2014 to December 2014 [18]. Samples are generated from breast tissue biopsy slides, stained with hematoxylin and eosin (HE). This database

contains microscopic images from the surgical biopsy (SOB) of breast tumors, otalizing 7,909 images divided into benign and malignant tumors, which have been collected at four different magnification factors (or zoom level, which is a term that we make use of interchangeably): 40×, 100×, 200× and 400×. Table 2 summarizes the image distribution of the dataset and Fig. 4(c). shows some samples of this dataset. This dataset is also available and can be downloaded from the web[3].

Table 2: Image distribution by magnification factor and class.

magnification	Benign	Malignant	Total
40×	625	1,370	1,995
100×	644`	1,437	2,081
200×	623	1,390	2,013
400×	588	1,232	1,820
Total	2,480	5,429	7,909
# Patients	24	58	82

3. 2. Accuracy Calculation

To enable comparison of the numerical results with other published methods on these datasets, different accuracy measures were used depending on the dataset. For the Kimia Path24 dataset, the evaluation metrics proposed in [16] were adopted. There are $n_{tot} = 1325$ testing patches P_s^j that belongs to 24 sets $\Gamma_S = \{P_S^j \mid s \in S, j = 1,2,...\}$ with $s = 0,1,\ldots,23$. Looking at the set of retrieved images for an experiment, R, the **patch-to-scan** accuracy, η_p, can be defined as:

$$\eta_p = \frac{1}{n_{tot}} \sum_{s \in S} |R \cap \Gamma_s| \qquad (10)$$

The **whole-scan accuracy,** η_w, can be defined as:

$$\eta_w = \frac{1}{24} \sum_{s \in S} |R \cap \Gamma_s| \qquad (11)$$

With the **total accuracy** is defined as $\eta_{total} = \eta_p \times \eta_w$.

For the BreakHis dataset, the **patient score** and global **recognition rate** were used, as described in [18]:

$$Patient\ \ Score = \frac{N_{rec}}{N_P} \qquad (12)$$

$$\text{Recognition Rate} = \frac{\sum patient\ score}{total\ number\ of\ patients} \qquad (13)$$

Where N_P is the number of cancer images of patient P and N_{rec} is the number images that are classified correctly for patient P.

3. 3. Numerical Results

Results for Kimia Path24 dataset- As a preprocessing step, all testing and training patches were normalized to the range [0, 1]. Variance (V), mean (M), and LVC features were extracted for circularly symmetric neighborhoods with (P, R) values of (8,1), (16,2), and (24,3) in the simulations. The V and M features were quantized into 16 levels (L = 16).

To determine the optimal threshold value for computing the LVC features, an additional experiment was conducted. Accuracy was evaluated on the Kimia Path960 dataset — a subset of the Kimia Path24 dataset containing 960 images — by varying the threshold value within the range [0, 1] in small increments.

Fig.6 illustrates how accuracy changes with respect to variations in the threshold. As shown, the highest accuracy (83.5%)

[3] https://web.inf.ufpr.br/vri/databases/breast-cancer-histopathological-database-breakhis/

was achieved using a threshold value of 0.1; therefore, T = 0.1 was selected for further experiments. The Path960 dataset is publicly available for download[4].

Both retrieval and classification approaches were considered. For the retrieval task, different distance measures such as L1 and L2 norms, X^2 (Chi-squared) were used to retrieve the most similar patch respect to the given test sample patch (query image) and for classification, an SVM was employed to

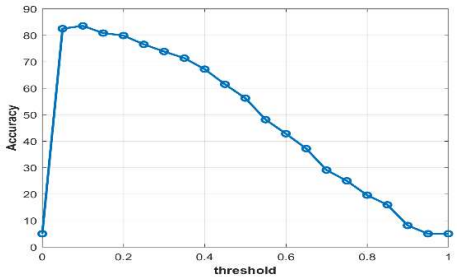

Fig.6. Accuracy changes for the Kimia path960 dataset with respect to threshold changes to find the optimal value for T in calculating LVC feature. For T=0.1 accuracy is 83.5%.

Determine the label of the patch most similar to the test sample. Table 3 shows the evaluation performances $\{\eta_p, \eta_w, \eta_{total}\}$ for different extracted local features and various combinations of these features in supervised and unsupervised approaches for cases I and II. In this table |h| is the dimension of the feature vector, and $h_{LBP^{riu2}}$, h_V, h_M and h_{LVC} refer to the concatenated $LBP^{riu2}{}_{V_{P,R}}$, $M_{P,R}$ and $LVC_{P,R}$ features with (P,R) values of (8,1), (16,2) and (24,3), for example

$h_{LBP^{riu2}} = [h_{LBP^{riu2}_{8,1}}, h_{LBP^{riu2}_{16,2}}, h_{LBP^{riu2}_{24,3}}]$.

As shown in Table 3 adding LVC feature to the LBP^{riu2}, V and M features has the greatest influence on the improving the evaluation performances. The best evaluation performance for all supervised and unsupervised approaches, was achieved for case II which has been highlighted in the table.

Feature selection for Kimia Path24 dataset- It was observed that although the addition of the mean intensity feature to the variance (V) and LVC features improved classification performance, in some WSIs, the number of correctly retrieved patches decreased based on the confusion matrix analysis. To address this issue and retain only the most discriminative features, several well-known feature selection methods were applied to the concatenated feature vectors formed from all local features (h= $h_{LBP^{riu2}} / h_V / h_{LVC} / h_M$). The selected methods included Laplacian score [19], multi-cluster feature selection (MCFS) [20], unsupervised discriminative feature selection (UDFS) [21], and correlation-based feature selection (CSF) [22]. The resulting reduced feature sets were then fed into an SVM classifier for evaluation on case II dataset. Fig. 7 illustrates the impact of feature vector dimensionality on retrieval accuracy at patch-level, whole-scan level, and scan-level using these feature selection approaches. The best performance was achieved using the MCFS method with k=140 selected features, yielding accuracies of {96.53%, 95.73%, 92.40%} across different evaluation levels.

[4] http://kimia.uwaterloo.ca/

Table 3: Evaluation performances $\{\eta_p, \eta_w, \eta_{total}\}$ for different extracted local features and various combinations of these features in supervised and unsupervised approaches for cases I and II.

h	|h|	L1 $\{\eta_p, \eta_w, \eta_{total}\}$	L2 $\{\eta_p, \eta_w, \eta_{total}\}$	X^2 $\{\eta_p, \eta_w, \eta_{total}\}$	SVM classifier $\{\eta_p, \eta_w, \eta_{total}\}$
$h_{LBP^{riu2}_{(8,1)}}$	10	I,{62.26%,58.19%,36.23%} II,{62.04%,59.23%,36.74%}	I,{62.04%,58.21%,36.11%} II,{61.96%,59.28%,36.73%}	I,{60.91%,57.11%,34.78%} II,{60.53%,57.59%,34.86%}	I,{72.83%,66.61%,48.51%} II,{72.98%,68.62%,50.08%}
$h_{LBP^{riu2}_{(16,2)}}$	18	I,{67.77%,63.67%,43.15%} II,{67.85%,65.18%,44.22%}	I,{65.58%,61.47%,40.31%} II,{65.81%,63.30%,41.66%}	I,{61.89%,57.3%,35.46%} II,{62.19%,59.42%,36.95%}	I,{77.28%,72.15%,55.76%} II,{77.66%,74.89%,58.16%}
$h_{LBP^{riu2}_{(24,3)}}$	26	I,{71.25%,67.22%,47.89%} II,{69.28%,66.90%,46.35%}	I,{71.55%,67.91%,48.59%} II,{70.57%,68.54%,48.36%}	I,{66.64%,62.45%,41.61%} II,{67.25%,64.57%,43.42%}	I,{77.66%,73.12%,56.79%} II,{77.96%,75.72%,59.03%}
$h_{LBP^{riu2}_{(8,1)}} / h_{LBP^{riu2}_{(16,2)}}$	28	I,{70.94%,67.06%,47.57%} II,{70.42%,67.63%,47.62%}	I,{69.43%,65.32%,45.35%} II,{69.21%,66.47%,46.00%}	I,{64.30%,60.66%,39.00%} II,{64.45%,61.71%,39.77%}	I,{86.49%,82.19%,71.09%} II,{87.32%,85.32%,74.50%}
$h_{LBP^{riu2}_{(8,1)}} / h_{LBP^{riu2}_{(24,3)}}$	36	I,{73.36%,69.52%,51.00%} II,{73.58%,71.43%,52.56%}	I,{71.02%,67.27%,47.78%} II,{71.40%,69.46%,49.59%}	I,{64.83%,61.29%,39.73%} II,{66.26%,63.99%,42.41%}	I,{88.00%,84.49%,74.35%} II,{88.22%,86.43%,76.25%}
$h_{LBP^{riu2}_{(16,2)}} / h_{LBP^{riu2}_{(24,3)}}$	44	I,{71.85%,67.73%,48.66%} II,{72.53%,70.55%,51.17%}	I,{71.47%,67.54%,48.27%} II,{71.54%,69.04%,49.40%}	I,{64.38%,60.18%,38.74%} II,{64.91%,62.50%,40.57%}	I,{86.57%,83.92%,72.65%} II,{86.19%,84.79%,73.08%}
$h_{LBP^{riu2}}$	54	I,{75.62%,71.30%,53.91%} II,{74.94%,72.48%,54.32%}	I,{ 71.85%,67.48%,48.48%} II,{71.92%,69.85%,50.24%}	I ,{65.13%,61.52%,40.07%} II,{65.74%,63.45%,41.71%}	I,{90.64%,87.80%,79.58%} II,{90.94%,89.62%,81.50%}
$h_{V_{(8,1)}}$	16	I,{30.79%,28.10%,8.65%} II,{30.64%,29.12%,8.92%}	I,{ 29.21%,26.68%,7.79%} II,{29.36%,28.15%,8.26%}	I ,{26.26%,23.71%,6.22%} II,{27.25%,26.22%,7.14%}	I,{34.94%,30.38%,10.62%} II,{33.21%,29.10%,9.26%}
$h_{V_{(16,2)}}$	16	I,{29.43%,25.30%,7.45%} II,{32.68%,30.68%,10.02%}	I,{ 28.00%,24.22%,6.78%} II,{31.17%,29.42%,9.17%}	I ,{26.19%,22.52%,5.90%} II,{28.68%,27.18%,7.80%}	I,{34.34%,29.74%,10.21%} II,{36.38%,32.85%,11.95%}
$h_{V_{(24,3)}}$	16	I,{31.92%,29.39%,9.38%} II,{31.70%,30.27%,9.60%}	I,{ 31.77%,29.08%,9.24%} II,{29.89%,28.48%,8.51%}	I ,{29.43%,26.65%,7.85%} II,{28.91%,27.05%,7.82%}	I,{36.22%,32.75%,11.86%} II,{36.38%,33.10%,12.04%}
$h_{V_{(8,1)}} / h_{V_{(16,2)}}$	32	I,{38.57%,32.97%,12.72%} II,{43.92%,41.94%,18.42%}	I,{ 35.62%,30.49%,10.86%} II,{40.68%,39.08%,15.90%}	I ,{32.22%,27.64%,8.91%} II,{36.15%,34.32%,12.41%}	I,{40.98%,35.08%,14.38%} II,{49.06%,45.22%,22.18%}
$h_{V_{(8,1)}} / h_{V_{(24,3)}}$	32	I,{44.98%,41.17%,18.52%} II,{44.00%,43.08%,18.95%}	I,{42.34%,38.71%,16.39%} II,{42.34%,41.15%,17.42%}	I ,{38.42%,34.93%,13.42%} II,{38.19%,36.20%,13.82%}	I,{53.06%,48.21%,25.58%} II,{52.45%,49.10%,25.75%}
$h_{V_{(16,2)}} / h_{V_{(24,3)}}$	32	I,{34.87%,29.80%,10.39%} II,{38.11%,36.77%,14.01%}	I,{33.66%,28.73%,9.67%} II,{36.38%,34.90%,12.70%}	I ,{30.79%,26.26%,8.59%} II,{33.13%,31.28%,10.37%}	I,{40.23%,34.46%,13.86%} II,{46.49%,44.04%,20.48%}
h_V	48	I,{39.92%,34.24%,13.67%} II,{45.43%,44.23%,20.09%}	I,{37.58%,32.17%,12.09%} II,{42.34%,41.15%,17.42%}	I,{33.58%,28.68%,9.63%} II,{38.04%,36.10%,13.73%}	I,{44.30%,37.78%,16.74%} II,{54.41%,51.30%,27.92%}
$h_{M_{(8,1)}}$	16	I,{59.47%,57.13%,33.97%} II,{60.16%,59.44%,35.75%}	I,{ 58.19%,56.20%,32.70%} II,{58.42%,58.48%,34.16%}	I ,{55.47%,53.31%,29.57%} II,{56.68%,57.17%,34.40%}	I,{72.53%,69.92%,50.72%} II,{72.38%,71.37%,51.66%}
$h_{M_{(16,2)}}$	16	I,{59.47%,57.13%,33.97%} II,{58.57%,58.26%,34.12%}	I,{ 58.19%,56.20%,32.70%} II,{56.98%,56.45%,8.26%}	I ,{55.47%,53.31%,29.57%} II,{54.26%,53.41%,28.98%}	I,{72.53%,69.92%,50.72%} II,{71.32%,70.45%,50.24%}
$h_{M_{(24,3)}}$	16	I,{59.47%,57.13%,33.97%} II,{55.85%,56.05%,31.31%}	I,{ 58.19%,56.20%,32.70%} II,{54.26%,54.37%,29.51%}	I ,{55.47%,53.31%,29.57%} II,{52.98%,52.23%,27.67%}	I,{72.53%,69.92%,50.72%} II,{67.92%,66.54%,45.20%}
$h_{M_{(8,1)}} / h_{M_{(16,2)}}$	32	I,{61.58%,59.43%,36.60%} II,{60.83%,59.60%,36.50%}	I,{60.23%,58.04%,34.95%} II,{58.94%,58.47%,34.47%}	I ,{59.17%,56.24%,33.28%} II,{59.55%,59.19%,35.24%}	I,{78.94%,75.86%,59.89%} II,{78.94%,78.54%,62.00%}
$h_{M_{(8,1)}} / h_{M_{(24,3)}}$	32	I,{63.17%,61.03%,38.55%} II,{63.54%,63.30%,40.22%}	I,{61.81%,59.77%,36.94%} II,{61.96%,61.75%,38.26%}	I ,{59.02%,56.60%,33.41%} II,{59.85%,59.63%,35.69%}	I,{80.38%,77.95%,62.66%} II,{80.83%,80.45%,62.03%}
$h_{M_{(16,2)}} / h_{M_{(24,3)}}$	32	I,{60.00%,57.61%,34.56%} II,{59.70%,59.69%,35.63%}	I,{60.15%,57.63%,34.67%} II,{59.09%,59.08%,34.90%}	I ,{56.68%,54.11%,30.67%} II,{57.13%,56.91%,32.52%}	I,{76.83%,73.99%,56.84%} II,{77.74%,76.98%,59.84%}
h_M	48	I ,{61.66%,59.49%,36.68%} II,{61.74%,61.63%,38.04%}	I,{61.21%,59.10%,36.17%} II,{61.06%,60.73%,37.08%}	I,{59.02%,56.55%,33.38%} II,{59.62%,59.54%,35.50%}	I,{80.00%,76.97%,61.58%} II,{80.60%,80.01%,64.49%}
$h_{LVC_{(8,1)}}$	6	I ,{40.38%,35.66%,14.40%} II,{39.62%,37.02%,14.67%}	I,{40.45%,35.54%,14.38%} II,{39.25%,36.69%,14.40%}	I,{39.47%,34.62%,13.67%} II,{38.04%,35.28%,13.42%}	I,{49.96%,43.52%,21.74%} II,{49.66%,44.42%,22.06%}
$h_{LVC_{(16,2)}}$	10	I ,{50.72%,46.08%,23.37%} II,{51.55%,49.38%,25.45%}	I,{59.51%,44.91%,22.23%} II,{52.08%,49.63%,25.84%}	I,{48.91%,44.02%,21.53%} II,{50.04%,47.53%,23.78%}	I,{62.49%,56.83%,35.52%} II,{63.77%,59.67%,38.05%}
$h_{LVC_{(24,3)}}$	14	I ,{54.71%,49.85%,27.28%} II,{54.72%,51.70%,28.29%}	I,{52.91%,48.34%,25.58%} II,{52.45%,49.00%,26.22%}	I,{49.06%,44.60%,21.88%} II,{49.89%,47.46%,23.68%}	I,{68.75%,63.26%,43.49%} II,{70.49%,67.14%,47.33%}
$h_{LVC_{(8,1)}} / h_{LVC_{(16,2)}}$	16	I ,{54.79%,49.49%,27.11%} II,{56.91%,54.00%,30.73%}	I,{55.02%,49.69%,27.34%} II,{57.66%,55.00%,31.71%}	I,{53.58%,48.18%,28.82%} II,{55.09%,52.44%,28.89%}	I,{69.43%,63.76%,44.27%} II,{70.57%,67.18%,47.40%}
$h_{LVC_{(8,1)}} / h_{LVC_{(24,3)}}$	20	I ,{57.66%,52.73%,30.40%} II,{58.19%,55.36%,32.21%}	I,{57.28%,52.23%,29.92%} II,{57.21%,54.35%,31.10%}	I,{52.98%,48.10%,25.48%} II,{54.34%,51.39%,27.93%}	I,{74.72%,69.89%,52.22%} II,{75.09%,72.19%,54.21%}
$h_{LVC_{(16,2)}} / h_{LVC_{(24,3)}}$	24	I ,{59.10%,54.28%,32.08%} II,{57.96%,54.63%,31.67%}	I,{56.30%,51.47%,28.98%} II,{57.28%,54.28%,31.10%}	I,{52.45%,47.79%,25.07%} II,{54.04%,51.17%,27.65%}	I,{75.40%,70.92%,53.47%} II,{75.92%,73.56%,55.85%}
h_{LVC}	30	I,{59.47%,54.52%,32.43%} II,{59.77%,56.76%,33.93%}	I,{58.49%,53.55%,31.32%} II,{59.25%,56.39%,33.41%}	I,{54.04%,49.19%,26.58%} II,{55.77%,52.80%,29.45%}	I,{77.66%,73.35%,56.97%} II,{77.58%,74.64%,57.91%}

Table 3(continue): Evaluation performances $\{\eta_p, \eta_w, \eta_{total}\}$ for different extracted local features and various combinations of these features in supervised and unsupervised approaches for cases I and II.

h	|h|	L1 $\{\eta_p, \eta_w, \eta_{total}\}$	L2 $\{\eta_p, \eta_w, \eta_{total}\}$	X^2 $\{\eta_p, \eta_w, \eta_{total}\}$	SVM classifier $\{\eta_p, \eta_w, \eta_{total}\}$
$h_{LBP^{riu2}} / h_V$	102	I,{74.87%,70.01%,52.48%} II,{78.19%,76.19%,59.57%}	I,{69.58%,63.75%,44.36%} II,{75.55%,73.65%,55.64%}	I,{60%,53.90%,32.34%} II,{66.87%,64.48%,43.11%}	I,{73.36%,64.75%,47.50%} II,{93.28%,91.72%,85.56%}
$h_{LBP^{riu2}} / h_M$	102	I,{81.74%,79.44%,64.93%} II,{78.91%,79.93%,64.67%}	I,{77.28%,74.83%,57.83%} II,{76.15%,75.11%,57.20%}	I,{72.38%,69.91%,50.60%} II,{72.38%,71.72%,51.91%}	I,{92.38%,89.89%,83.04%} II,{92.91%,92.43%,85.87%}
$h_{LBP^{riu2}} / h_{LVC}$	84	I,{78.94%,75.06%,59.25%} II,{77.89%,75.47%,64.67%}	I,{75.55%,72.0%,54.40%} II,{75.47%,73.20%,55.24%}	I,{69.81%,66.10%,46.15%} II,{69.51%,66.61%,46.30%}	I,{94.26%,92.42%,87.12%} II,{94.19%,92.85%,87.46%}
h_V / h_M	96	I,{65.81%,62.76%,41.30%} II,{68.08%,67.56%,45.99%}	I,{64.38%,61.52%,39.61%} II,{65.81%,65.14%,42.87%}	I,{59.70%,56.25%,33.58%} II,{62.72%,62.27%,39.05%}	I,{71.62%,67.22%,48.14%} II,{84.60%,83.18%,70.37%}
h_V / h_{LVC}	78	I,{59.92%,53.04%,31.79%} II,{65.81%,62.99%,41.46%}	I,{53.98%,49.90%,28.43%} II,{63.17%,60.34%,38.12%}	I,{52.30%,45.28%,23.68%} II,{59.55%,56.29%,33.52%}	I,{62.79%,53.52%,33.61%} II,{83.47%,81.48%,68.02%}
$h_{LBP^{riu2}} / h_V / h_M$	150	I,{81.66%,78.80%,64.35%} II,{82.19%,81.41%,66.91%}	I,{77.89%,75.0%,58.41%} II,{77.66%,76.57%,59.46%}	I,{70.42%,67.12%,47.27%} II,{73.66%,72.95%,53.73%}	I,{83.62%,79.47%,66.45%} II,{93.13%,92.52%,86.16%}
$h_V / h_M / h_{LVC}$	126	I,{73.13%,69.55%,50.87%} II,{74.64%,73.51%,54.87%}	I,{69.89%,66.36%,46.37%} II,{71.55%,70.39%,50.36%}	I,{65.89%,62.57%,41.23%} II,{68.83%,68.02%,46.82%}	I,{79.62%,75.20%,59.88%} II,{90.19%,88.95%,80.22%}
$h_{LBP^{riu2}} / h_V / h_{LVC}$	132	I,{77.36%,73.02%,56.49%} II,{80.15%,78.22%,62.69%}	I,{73.66%,69.05%,50.87%} II,{76.52%,74.60%,57.09%}	I,{64.53%,58.59%,37.81%} II,{70.04%,67.89%,47.55%}	I,{77.43%,69.65%,53.93%} II,{95.25%,94.03%,89.56%}
$h_{LBP^{riu2}} / h_V / h_{LVC} / h_M$	180	I,{82.72%,79.65%,65.88%} **II,{83.70%,82.48%,69.04%}**	I,{79.92%,76.70%,61.30%} **II,{79.85%,78.50%,62.68%}**	I,{72.60%,69.55%,50.50%} **II,{74.64%,73.62%,54.95%}**	I,{86.64%,82.86%,71.79%} **II,{94.64%,93.85%,88.82%}**

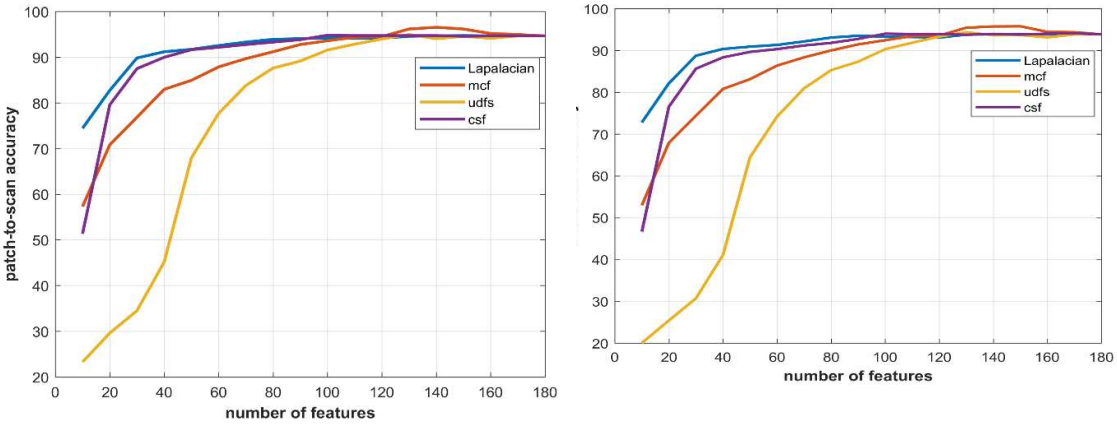

(a). patch-to-scan accuracy. (b). whole-scan accuracy.

Fig.7. Effect of chosen number of features to patch-to-scan accuracy (a), whole-scan accuracy (b) for different feature selection methods for the Kimia path24 dataset.

Comparative Analysis Using the Kimia Path24 Dataset- The proposed method was compared with other approaches reported in the literature. Table 4 presents the evaluation performance of various methods applied to this dataset. The number of extracted training patches is also included to provide a comprehensive comparison. Compared to other methods, the proposed approach achieves higher image retrieval accuracy with a lower-dimensional feature vector. All experiments in this study were conducted in a MATLAB environment on a system with a 2.60 GHz CPU, eight cores, and 16 GB of RAM.

Table 4: Evaluation performance for various methods for Kimia Path24 dataset.

Method	Accuracy $\{\eta_p, \eta_w, \eta_{total}\}$	|h|	# training patches
Proposed method(case II)	**{96.5%, 95.7%, 92.4%}**	**140**	**30946**
Proposed method(caseI)	**{91.4%,88.60%,80.9%}**	**140**	**25979**
$ELP_{(10,d)}$[23]	{82.7%, 79.9%, 66.1%}	1024	27055
$ELP_{(10,m)}$[23]	{82.3%, 79.3%, 65.3%}	256	27055
VGC_{FC7}[23]	{79.5%, 76.9%, 61.1%}	4096	n.a.
$LBP_{(24,2)}$[23]	{77.8%, 73.3%, 57.0%}	555	27055
VGG_{pool}[23]	{72.5%, 67.2%, 48.7%}	6272	n.a.
CNN [24]	{65.0%, 64.8%, 42.1%}	1024	40,513
BoVW[24]	{65.0%, 61.0%, 39.7%}	800	27055

Results for the BreakHis Dataset – The dataset contains four histologically distinct types of benign breast tumors: adenosis (A), fibroadenoma (F), phyllodes tumor (PT), and tubular adenoma (TA), as well as four types of malignant breast tumors: ductal carcinoma (DC), lobular carcinoma (LC), mucinous carcinoma (MC), and papillary carcinoma (PC). All images are provided in 3-channel RGB format with a resolution of 700×460 pixels. The dataset was randomly divided into training (70%) and testing (30%) subsets.

Normalization was applied, and local low-level features were extracted from each color channel using radius {1,2,3} and neighborhood points{8,16,24}, with a threshold T= 0.1. The global recognition rate was used as the performance metric. Key results are presented in Table 5, with the best outcomes highlighted.

Table 5: Evaluation performance (recognition rate) for BreakHis dataset.

	Magnification factor											
	40X			**100X**			**200X**			**400X**		
Method	L1%	L2%	SVM %	L1%	L2%	SVM %	L1%	L2%	SVM %	L1%	L2%	SVM %
$h_{LBP^{riu2}}$	75.16	74.07	81.91	**75.50**	**74.62**	**84.23**	71.25	73.42	83.43	71.79	68.63	78.46
h_V	66.38	65.53	73.92	60.92	63.04	67.91	66.24	67.26	71.01	63.73	62.49	70.29
h_M	63.26	64.91	69.89	69.19	68.37	68.62	73.42	72.05	80.03	69.45	69.56	80.03
h_{LVC}	71.27	70.12	83.01	71.99	70.86	73.36	71.05	68.23	80.98	69.25	67.30	76.46
$h_{LBP^{riu2}} / h_V$	76.41	75.57	78.26	67.27	70.19	80.00	74.31	72.96	83.21	**73.11**	**73.31**	**80.84**
$h_{LBP^{riu2}} / h_M$	66.79	65.37	71.54	71.06	70.21	72.00	75.51	73.68	80.02	73.09	70.74	78.10
$h_{LBP^{riu2}} / h_{LVC}$	71.93	72.22	83.13	71.86	68.82	81.29	71.01	69.18	83.19	71.42	72.49	77.29
h_V / h_M	61.39	63.49	67.89	66.87	67.30	65.72	70.58	70.94	78.84	69.55	69.06	78.88
h_V / h_{LVC}	74.46	73.58	80.97	71.12	71.10	75.46	74.49	75.24	78.64	71.42	71.19	77.87
h_M / h_{LVC}	67.26	67.34	68.60	68.17	65.88	72.02	71.55	70.54	80.87	68.05	66.68	75.57
$h_{LBP^{riu2}} / h_M / h_V$	66.70	62.99	67.99	67.98	68.03	73.07	75.92	73.77	80.27	72.53	71.04	77.91
$h_{LBP^{riu2}} / h_M / h_{LVC}$	66.77	67.70	69.38	68.49	65.79	73.57	73.28	72.24	79.57	72.91	71.99	76.80
$h_{LBP^{riu2}} / h_V / h_{LVC}$	**78.00**	**75.34**	**84.44**	71.73	71.82	78.83	**71.74**	**73.56**	**83.44**	71.48	71.76	78.87
$h_V / h_M / h_{LVC}$	70.88	67.96	72.46	69.03	67.42	73.13	71.79	72.85	78.81	72.58	70.49	76.55
$h_{LBP^{riu2}} / h_V / h_{LVC} / h_M$	70.62	69.04	72.57	68.52	68.23	74.39	73.23	73.25	79.38	74.72	72.12	77.83

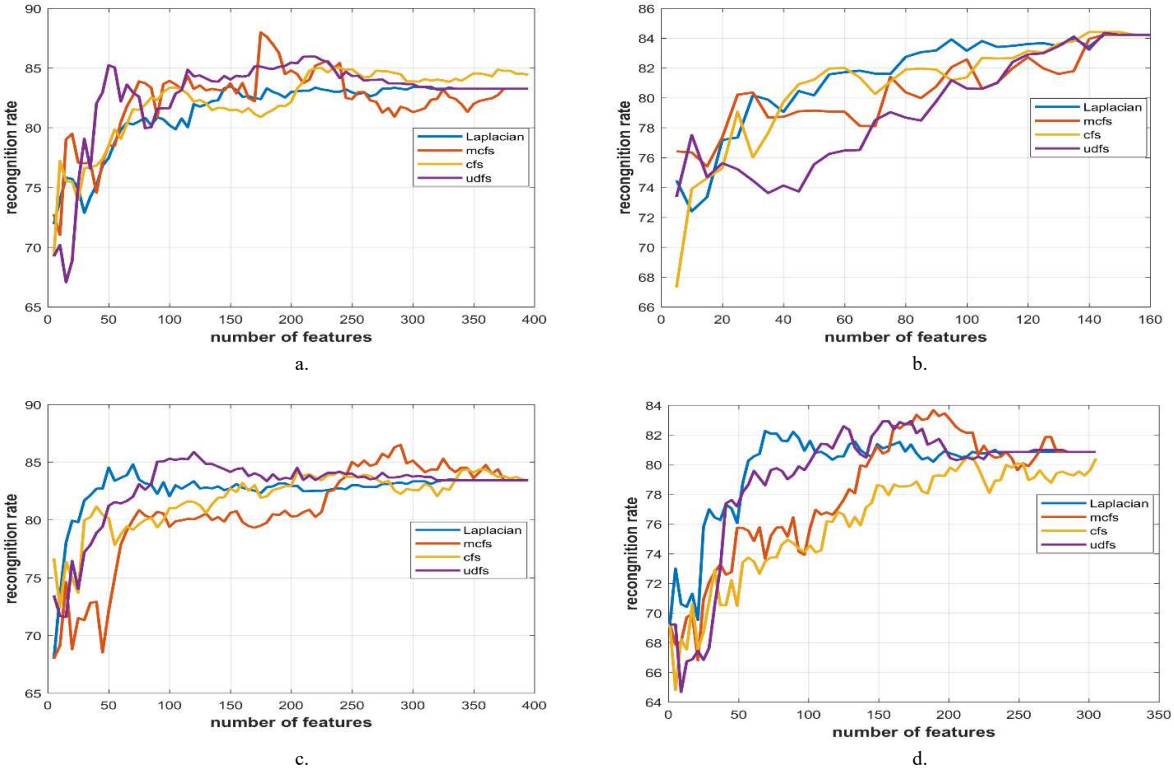

Fig.8. Effect of chosen number of features to recognition rate accuracy over the magnification factors, (a), 40X (b) 100X, (c) 200X ,(d) 400X for BreakHis dataset using different feature selection methods.

Table 6: Evaluation performance for various methods for BreakHis dataset.

Method	40X	100X	200X	400X
CLBP[18]	77.4%	76.4%	70.2%	72.8%
LPQ [18]	73.8%	72.8%	74.3%	73.7%
GLCM[18]	74.7%	78.6%	83.4%	73.7%
QRB[18]	74.4%	69.4%	69.6%	67.6%
PFTAS[18]	83.8%	82.1%	85.1%	82.3%
CNN [25]	84.0%	83.9%	86.3%	82.1%
CNN & Fusion Rules [26]	90.0%	88.4%	84.6%	86.1%
Proposed method	**88.00%**	**84.4%**	**86.5%**	**83.6%**

Feature selection for BreakHis dataset- To further improve classification accuracy and reduce the dimensionality of the feature vector, several feature selection methods—Laplacian Score, MCFS, UDFS, and CSF—were applied to the combination of features that yielded the best classification performance. The impact of selecting the most discriminative features on evaluation performance was assessed using an SVM classifier. Fig.8 illustrates the effect of feature vector dimensionality (i.e., the number of selected features) on classification performance (recognition rate) across different magnification factors and feature selection methods. The best results are {175,87.98%,mcfs},{140,84.41%,cfs} ,{290,56.50%,mcfs}, {189,83.64%,mcfs} over 40X ,100X, 200X and 400X magnification factors respectively where the first number is the dimension of the feature vector, the second number is the maximum recognition rate and the feature selection method that best result is achieved is the third one.

Comparative Analysis Using the BreakHis dataset- The best results were compared with other reported methods in the literature. Table 6 presents this comparison. As shown, the proposed method achieves higher classification accuracy than several existing approaches on the same dataset.

4. Summery and Conclusion

'n' this study, four low-level local features — rotation-invariant local binary pattern (LBP), mean intensity, variance, and local variation code (LVC) — were extracted from circular neighborhoods around the central pixel using various radii. These features were employed to address content-based medical image retrieval in histopathological images. The extracted features are invariant to rotation and grayscale shifts, enabling robust representation of texture patterns.

The impact of each individual feature and their combinations was evaluated using both supervised and unsupervised classification approaches on three publicly available datasets: Kimia Path24 and BreakHis. Experimental results demonstrated that, for one of the datasets, a single feature type was sufficient to achieve high classification accuracy. Moreover, different concatenation strategies were tested, and the results indicated that combining multiple feature types improved the modeling of micro-pattern structures, particularly for two of the datasets.

Feature selection methods were applied to the extracted feature vectors, which not only enhanced classification performance but also reduced the dimensionality of the feature space. Compared to previously proposed techniques, the presented method achieves higher accuracy with a more compact feature representation.

REFERENCES

[1] M. K. K. Niazi, A. V. Parwani, and M. N. Gurcan, "Digital pathology and artificial intelligence," The Lancet Oncology, vol. 20, no. 5, pp. e253–e261, May 2019.

[2] S. W. Jahn, M. Plass, and F. Moinfar, "Digital pathology: advantages, limitations and emerging perspectives," Journal of Clinical Medicine, vol. 9, no. 11, p. 3697, 2020.

[3] M. G. Hanna and M. H. Hanna, "Current applications and challenges of artificial intelligence in pathology," Human Pathology Reports, vol. 27, p. 300596, 2022.

[4] M. N. Gurcan, L. E. Boucheron, A. Can, A. Madabhushi, N. M. Rajpoot, and B. Yener, "Histopathological image analysis: A review," IEEE Reviews in Biomedical Engineering, vol. 2, pp. 147–171, 2009.

[5] E. A. Rakha, M. Toss, S. Shiino, P. Gamble, R. Jaroensri, C. H. Mermel, and P. H. C. Chen, "Current and future applications of artificial intelligence in pathology: a clinical perspective," Journal of Clinical Pathology, vol. 74, no. 7, pp. 409–414, 2021.

[6] A. Madabhushi and G. Lee, "Image analysis and machine learning in digital pathology: Challenges and opportunities," Medical Image Analysis, vol. 33, pp. 170–175, 2016.

[7] S. B. Mukadam and H. Y. Patil, "Machine learning and computer vision based methods for cancer classification: A systematic review," Archives of Computational Methods in Engineering, vol. 31, no. 5, pp. 3015–3050, 2024.

[8] A. Latif, A. Rasheed, U. Sajid, J. Ahmed, N. Ali, N. I. Ratyal, B. Zafar, S. H. Dar, M. Sajid, and T. Khalil, "Content-based image retrieval and feature extraction: A comprehensive review," Mathematical Problems in Engineering, vol. 2019, no. 1, p. 9658350, 2019.

[9] M. Heikkilä, M. Pietikäinen, and C. Schmid, "Description of interest regions with local

binary patterns," Pattern Recognition, vol. 42, no. 3, pp. 425–436, 2009.

[10] D. G. Lowe, "Distinctive image features from scale-invariant keypoints," International Journal of Computer Vision, vol. 60, pp. 91–110, 2004.

[11] H. Bay, A. Ess, T. Tuytelaars, and L. Van Gool, "Speeded-up robust features (SURF)," Computer Vision and Image Understanding, vol. 110, no. 3, pp. 346–359, 2008.

[12] N. Dalal and B. Triggs, "Histograms of oriented gradients for human detection," in Proc. 2005 IEEE Computer Society Conf. on Computer Vision and Pattern Recognition.

[13] T. Ojala, M. Pietikäinen, and D. Harwood, "A comparative study of texture measures with classification based on featured distributions," Pattern Recognition, vol. 29, no. 1, pp. 51–59, 1996.

[14] Ş. Öztürk and A. Bayram, "Comparison of HOG, MSER, SIFT, FAST, LBP and CANNY features for cell detection in histopathological images," Helix, vol. 8, no. 3, pp. 3321–3325, 2018.

[15] T. Ojala, M. Pietikäinen, and T. Maenpaa, "Multiresolution gray-scale and rotation invariant texture classification with local binary patterns," IEEE Transactions on Pattern Analysis and Machine Intelligence, vol. 24, no. 7, pp. 971–987, 2002.

[16] M. Babaie, S. Kalra, A. Sriram, C. Mitcheltree, S. Zhu, S. Khatami, A. Rahnamayan, and H. Tizhoosh, "Classification and retrieval of digital pathology scans: A new dataset," in Proc. Workshop on Computer Vision for Microscopy Image Analysis (CVMI), IEEE Conf. on Computer Vision and Pattern Recognition (CVPR), pp. 8–16, 2017.

[17] A. Jurio, H. Bustince, M. Pagola, P. Couto, and W. Pedrycz, "New measures of homogeneity for image processing: An application to fingerprint segmentation," Soft Computing, vol. 18, no. 6, pp. 1055–1066, 2014.

[18] F. Spanhol, L. S. Oliveira, C. Petitjean, and L. Heutte, "A dataset for breast cancer histopathological image classification," IEEE Transactions on Biomedical Engineering, vol. 63, no. 7, pp. 1455–1462, 2015.

[19] X. He, D. Cai, and P. Niyogi, "Laplacian score for feature selection," in Proc. Int. Conf. on Neural Information Processing Systems (NIPS), pp. 507–514, 2005.

[20] D. Cai, C. Zhang, and X. He, "Unsupervised feature selection for multi-cluster data," in Proc. ACM Int. Conf. on Knowledge Discovery and Data Mining (KDD), pp. 333–342, 2010.

[21] Y. Yang, H. T. Shen, Z. Ma, Z. Huang, and X. Zhou, "Norm regularized discriminative feature selection for unsupervised learning," in Proc. 22nd Int. Joint Conf. on Artificial Intelligence (IJCAI), pp. 1589–1594, 2011.

[22] M. Hall, "Correlation-based feature selection for machine learning," Ph.D. dissertation, Dept. of Computer Science, Univ. of Waikato, Hamilton, New Zealand, 1999.

[23] H. R. Tizhoosh and M. Babaie, "Representing medical images with encoded local projections," IEEE Transactions on Biomedical Engineering, vol. 65, no. 10, pp. 2267–2277, 2018.

[24] B. Kieffer, M. Babaie, S. Kalra, and H. R. Tizhoosh, "Convolutional neural networks for histopathology image classification: Training vs. using pre-trained networks," in Proc. 2017 Seventh Int. Conf. on Image Processing Theory, Tools and Applications (IPTA), pp. 1–6, Nov. 2017.

[25] F. A. Spanhol, L. S. Oliveira, P. R. Cavalin, C. Petitjean, and L. Heutte, "Deep features for breast cancer histopathological image classification," in Proc. 2017 IEEE International Conference on Systems, Man, and Cybernetics (SMC), pp. 1868–1873, Oct. 2017.

[26] F. A. Spanhol, L. S. Oliveira, C. Petitjean, and L. Heutte, "Breast cancer histopathological image classification using convolutional neural networks," in Proc. 2016 International Joint Conference on Neural Networks (IJCNN), pp. 2560–2567, July 2016.